Bioarmor-Inspired 3D Electrodes for High-Capacitance Stretchable Supercapacitors

Chong Bai, Qianying Lu, Ting Fang, Lin Wang, Sisi Li, Yong Lin, Yan-qing Lu,* and Desheng Kong*

Stretchable supercapacitors are crucial for powering the next generation of wearable devices, but they face the challenge of insufficient areal capacitance. Although 3D electrodes improve the amount of active materials, their considerable thickness can increase stiffness and restrict deformability. Inspired by Armadillo's armor that incorporates rigid bony plates within elastic skin for optimal protection and flexibility, this study presents a 3D electrode designed to balance these conflicting requirements. The electrode comprises an array of densely packed, porous conductive pillars anchored to a soft current collector, effectively decoupling electrochemical and mechanical functions. The 900 μm-thick pillars act as a porous scaffold, enabling high loading of active material PEDOT at 10 mg cm^{-2}. Meanwhile, the current collector efficiently dissipates applied tension, resulting in exceptional deformability for the electrode. To demonstrate their practical application, these supercapacitors are integrated into a soft, untethered electronic system featuring a wireless charging circuit with a skin-conformal LED array for sustained operation. By effectively addressing the longstanding challenge of balancing high capacitance with mechanical compliance, this bioinspired electrode design establishes a transformative approach to create high-performance, deformation-resilient energy storage devices for wearable technologies.
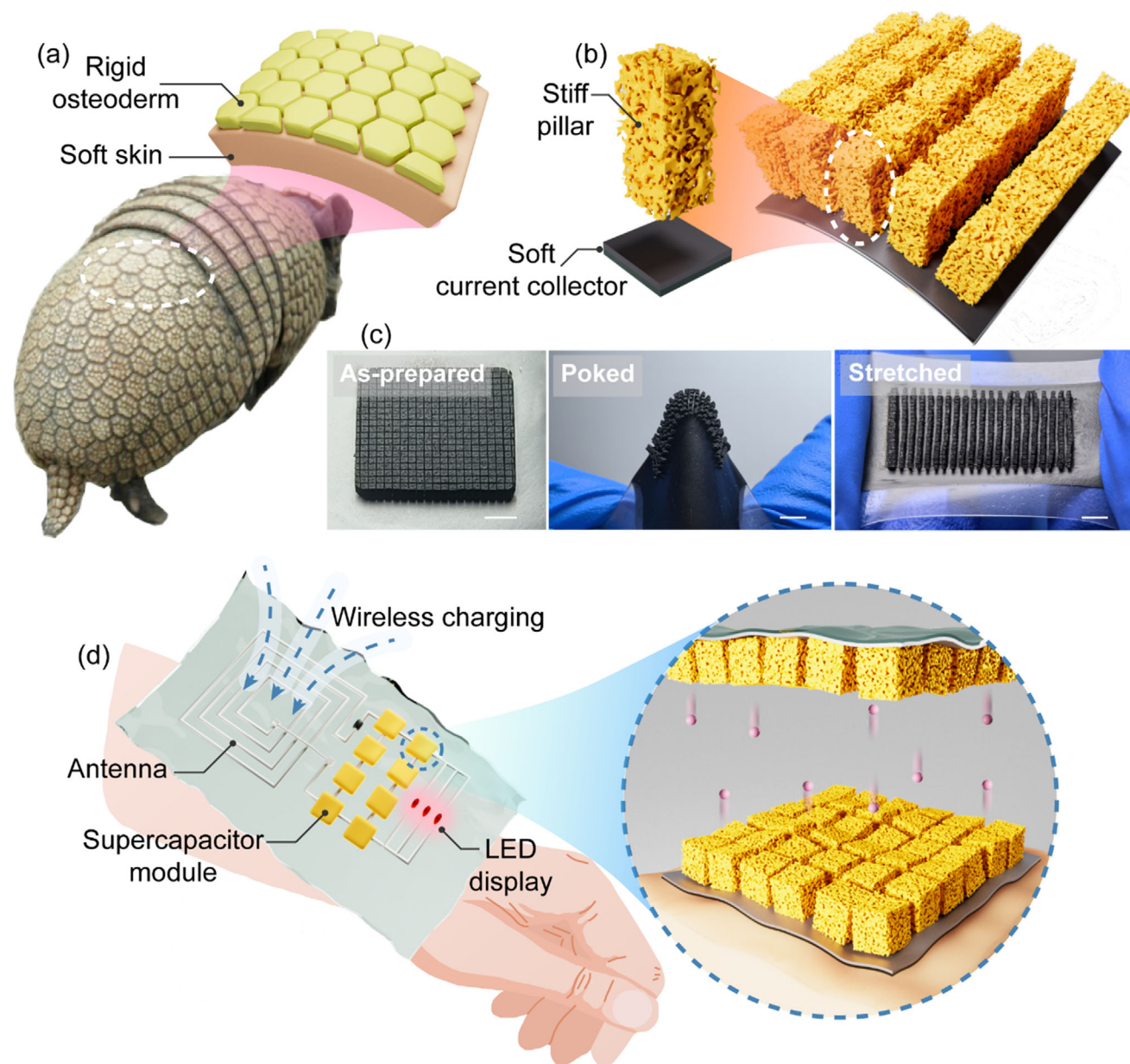
C. Bai, Q. Lu, T. Fang, L. Wang, S. Li, Y. Lin, D. Kong
State Key Laboratory of Analytical Chemistry for Life Science
Jiangsu Key Laboratory of Artificial Functional Materials
Nanjing University
Nanjing 210021, China
E-mail: dskong@nju.edu.cn
C. Bai, Q. Lu, T. Fang, L. Wang, S. Li, Y. Lin, Y.-qing Lu, D. Kong
College of Engineering and Applied Sciences
National Laboratory of Solid State Microstructures
Collaborative Innovation Center of Advanced Microstructures
Nanjing University
Nanjing 210093, China
E-mail: yqlu@nju.edu.cn
Y.-qing Lu, D. Kong
Key Laboratory of Intelligent Optical Sensing and Manipulation
Nanjing University
Nanjing 210093, China

1. Introduction

The rapid advancement of stretchable electronics holds transformative potential for future wearables, robotics, and human-machine interfaces.[1–4] Compliant mechanical properties are essential for these cutting-edge applications, enabling seamless integration with curved and dynamic surfaces.[5,6] Despite significant progress, the practical deployment of stretchable electronics often hinges on the availability of compatible energy storage solutions for portable, untethered device and circuit systems.[7–11] Among various options, stretchable supercapacitors are well-suited for powering these devices due to their rapid charge-discharge kinetics, long lifespan, and high power density.[12–15] Aqueous electrochemistries have additional advantages in this context, providing inherent non-flammability and enhanced safety for skin contact applications.[16–18]

Current design strategies for stretchable supercapacitors can be categorized into two main approaches. The first employs strain engineering to transform rigid thin-film electrodes into highly extensible structures, such as wrinkled surfaces, Kirigami-inspired patterns, and twisted fiber networks.[19–26] These designs enhance the stretchability of the devices by redistributing tensile stresses through mechanisms like global bending or out-of-plane buckling. The second strategy focuses on intrinsically stretchable electrodes, where active materials are blended with elastomeric matrices to form compliant composites.[27–30] Despite these advancements, both approaches face a persistent challenge: the inherent trade-off between achieving high capacitance and maintaining mechanical compliance. Thin-film electrodes suffer from an insufficient energy storage capacity due to low active material loading (≤ 5 mg cm^{-2}) constrained by the charge transport limit. Hierarchical 3D porous electrodes have emerged as a promising solution to this issue.[31–34] Their porous architecture of high surface area creates continuous conductive networks for electron and ion transport, allowing efficient utilization of active materials even in extremely thick electrodes.[35,36] Nevertheless, the improved electrochemical performance of 3D electrodes through increased mass loading often results in enhanced mechanical stiffness. Upon stretching,

**ADVANCED
SCIENCE NEWS**

www.advancedsciencenews.com

**ADVANCED
FUNCTIONAL
MATERIALS**

www.afm-journal.de

Figure 1. Bioarmor-inspired 3D electrodes for stretchable supercapacitors. a) Armadillo's dermal armor consists of packed bony plates attached to the soft skin tissue, which provides both protection and flexibility. b) Schematic illustration of the bioinspired 3D electrode design. c) Optical images demonstrating skin-like deformability of the bioinspired electrodes under poking and stretching manipulation. Scale bars: 2 mm. d) Integration of stretchable supercapacitors into body-worn electronic systems as reliable energy sources.

the structural issues of the electrodes manifest as fracture and interfacial delamination.[37] Consequently, it remains a fundamental challenge to realize both robust mechanical deformability and high electrochemical performance.

Biological systems, refined through millennia of evolution, provide elegant solutions to complex engineering challenges. A notable example is the armadillo's dermal armor that comprises densely packed fine bony plates anchored within soft skin tissues (**Figure 1a**).[38] This natural design strikes an exceptional balance between strong puncture resistance and mechanical flexibility.[39,40] Inspired by this concept, flexible protective gears

have been developed that incorporate discrete miniaturized armor plates arranged within soft substrates, significantly enhancing wearability without sacrificing performance.[41] These advancements underscore the potential of bioinspired architectures to integrate rigid material components into highly deformable systems. Extending this principle to stretchable energy storage could further enable the use of high-capacitance electrode designs, an area that remains largely unexplored.

In this work, we present a bioarmor-like 3D electrode design that concurrently delivers high capacitance and exceptional stretchability for wearable supercapacitors. By mimicking the

**ADVANCED
SCIENCE NEWS**

www.advancedsciencenews.com

**ADVANCED
FUNCTIONAL
MATERIALS**

www.afm-journal.de

armadillo's dermal armor, the electrode incorporates an array of stiff, vertically aligned pillars anchored to a soft current collector (see Figure 1b). This design effectively decouples mechanical deformability from electrochemical performance: the porous pillars boost charge storage capacity, while the compliant substrate accommodates mechanical stresses during large deformations. The as-prepared 3D electrodes can easily accommodate diverse mechanical manipulations like poking and stretching, as shown in Figure 1c. This electrode features a hierarchical architecture measuring 900 µm in thickness, enabling the enhanced loading of the poly(3,4-ethylenedioxythiophene) (PEDOT) active material at 10 mg cm^{-2}. The corresponding symmetric supercapacitor achieves a high areal capacitance of 244.5 mF cm^{-2} and over 95.5% retention of its initial capacitance at 100% tensile strain. To validate the practical utility, we have developed a wearable electronic system by integrating a wireless-charging-enabled supercapacitor module with a stretchable LED display, showcasing robust performance as a skin-attached energy source (Figure 1d). This bioinspired electrode design overcomes the traditional trade-off between areal capacitance and mechanical compliance, establishing a new paradigm for deformable energy storage devices in next-generation wearable technologies.

2. Results and Discussion

Figure 2a schematically depicts the fabrication process of the bioarmor-inspired electrode. Briefly, the multiwall carbon nanotubes (CNTs) and poly(styrene-ethylene-butylene-styrene) (SEBS) elastomer mixture has been further blended with salicylic acid microrods as the porogen to create a thick composite film (Figure S1, Supporting Information). This film is then shaped into well-defined pillars using selective laser ablation.[42–44] Subsequently, these pillars are thermally welded to a nanocomposite current collector inside a vacuum laminator. The tackified elastomer matrix, combined with applied heat and pressure, establishes a robust interfacial bond through polymer chain interdiffusion.[45,46] After evaporating salicylic acid under elevated temperatures, a hierarchical porous architecture is formed within these pillars, establishing bicontinuous pathways that facilitate efficient electrolyte infiltration. We opt for this assembly process over direct laser ablation of a pre-bonded composite due to the practical challenge of controlling ablation depth precisely without damaging the current collector. To enhance energy storage performance, the porous pillars are finally coated with poly(3,4-ethylenedioxythiophene) (PEDOT) by electrodeposition. PEDOT is a widely used conductive polymer for capacitive energy storage, prized for decent specific capacitance, excellent stability, and biocompatibility.[47,48]

The electrode incorporates a bilayer current collector composed of CNTs and silver nanowires (AgNWs) embedded within an elastomer matrix. The high-aspect-ratio nanofillers form 3D percolation networks inside the current collector, resulting in a low sheet resistance of 0.12 Ω sq^{-1} (Figure S2, Supporting Information). This resistance increases progressively during stretching, reaching 5.37 Ω at 100% strain. Additionally, the current collector also exhibits excellent mechanical durability, preserving a relatively low sheet resistance of 2.12 Ω sq^{-1} even after 1000 stretching cycles to 50% strain. Notably, the electrochemically sensitive AgNW layer 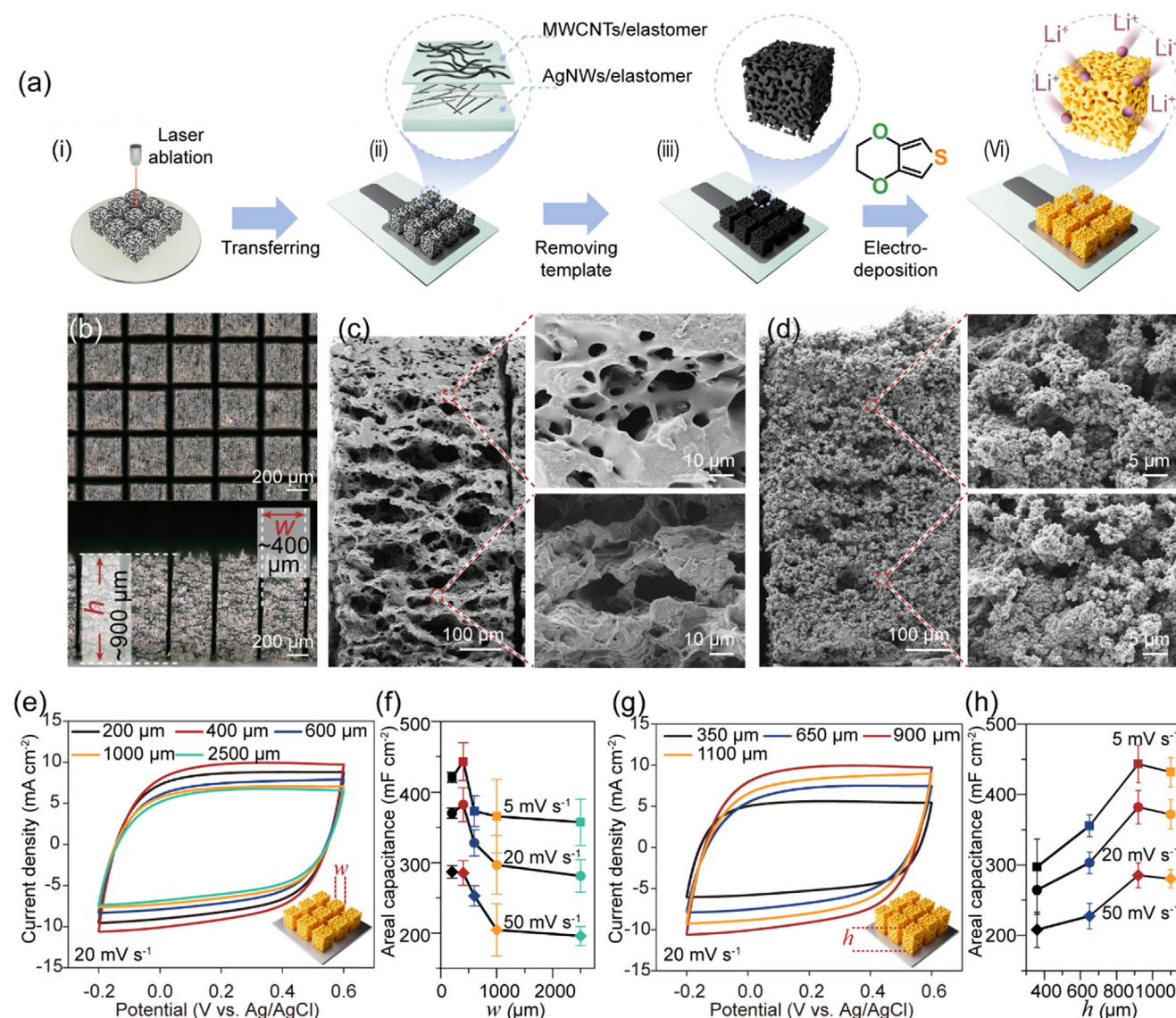is encapsulated by CNT nanocomposite in this bilayer structured current collector. The corresponding linear sweep voltammetry curve reveals a wide electrochemical stability window of ≈1.8 V in an aqueous 1 M LiCl electrolyte (Figure S3, Supporting Information). This bilayer design prevents the direct contact of AgNWs to the electrolyte, thereby suppressing their potential for corrosion. Moreover, this electrochemical stability is well preserved even after repeated mechanical deformation, underscoring the robustness of the current collector design.

The optical images reveal uniformly structured square pillars, each ≈400 µm in width and 900 µm in thickness, mounted on the current collector (see Figure 2b). These structures are created via layer-by-layer laser ablation, allowing for the facile fabrication of high-aspect-ratio designs.[43] As illustrated in Figure 2c and Figure S4 (Supporting Information), the pillars feature a porous microstructure that is consistently distributed from the top surface to the base. Magnified SEM images show 3D, interconnected pores that are tens of micrometers in size. This architecture has pores that can be filled with electrolytes, facilitating rapid ion diffusion throughout thick electrodes.[49,50] Subsequently, PEDOT is applied to the porous scaffold of the pillars through electrodeposition, acting as the active material. CNTs are co-deposited as biocompatible nanofillers to enhance electronic conductivity within the composite and increase its surface area.[51,52] In Figure 2d and Figure S5 (Supporting Information), SEM images of the resulting hierarchical 3D architecture show a highly textured PEDOT nanocomposite coated on these porous pillars. Energy dispersive spectroscopy analyses in Figure S6 (Supporting Information) confirm the uniform distribution of sulfur and oxygen (PEDOT indicators) across the pillars, further validating homogeneous deposition. Although Brunauer−Emmett−Teller (BET) analysis indicates a reduction in surface area after PEDOT deposition, a significant volume of nanoporosity is retained within the framework (Figure S7, Supporting Information). These residual nanopores sustain abundant active sites, which are crucial for capacitive energy storage.[53,54] Collectively, these findings highlight the promising potential of the 3D hierarchical electrodes for achieving high areal capacitance.

The electrochemical performance of these bioarmor-inspired ultrathick electrodes is systematically evaluated in a three-electrode configuration using a 1 M LiCl aqueous electrolyte. Figure 2e presents the CV measurements of electrodes that exhibit symmetric, quasi-rectangular shapes, indicating ideal capacitive behavior.[55] Symmetrical GCD profiles with linear slope further confirm their excellent capacitive characteristics (refer to Figure S8, Supporting Information). Figure 2f summarizes the average areal capacitance as a function of pillar width. Areal capacitance initially increases with expanding pillars and peaks at a pillar width of 400 µm, attributed to their increased geometric coverage. Beyond this threshold, the areal capacitance gradually declines as the pillars widen, due to elongated diffusion pathways that hinder active material deposition and charge-discharge processes.[56] Similar trends are noted in CV measurements across different rates, although notable deviations from rectangularity emerge at 50 mV s^{-1} due to overpotential effects (Figure S9, Supporting Information).

The effects of pillar thickness are also examined. Capacitive behavior is evident from the quasi-rectangular CV curves and triangular GCD profiles across different thicknesses (see Figure 2g and Figure S10, Supporting Information). As shown in Figure 2h,

ADVANCED
SCIENCE NEWS

www.advancedsciencenews.com
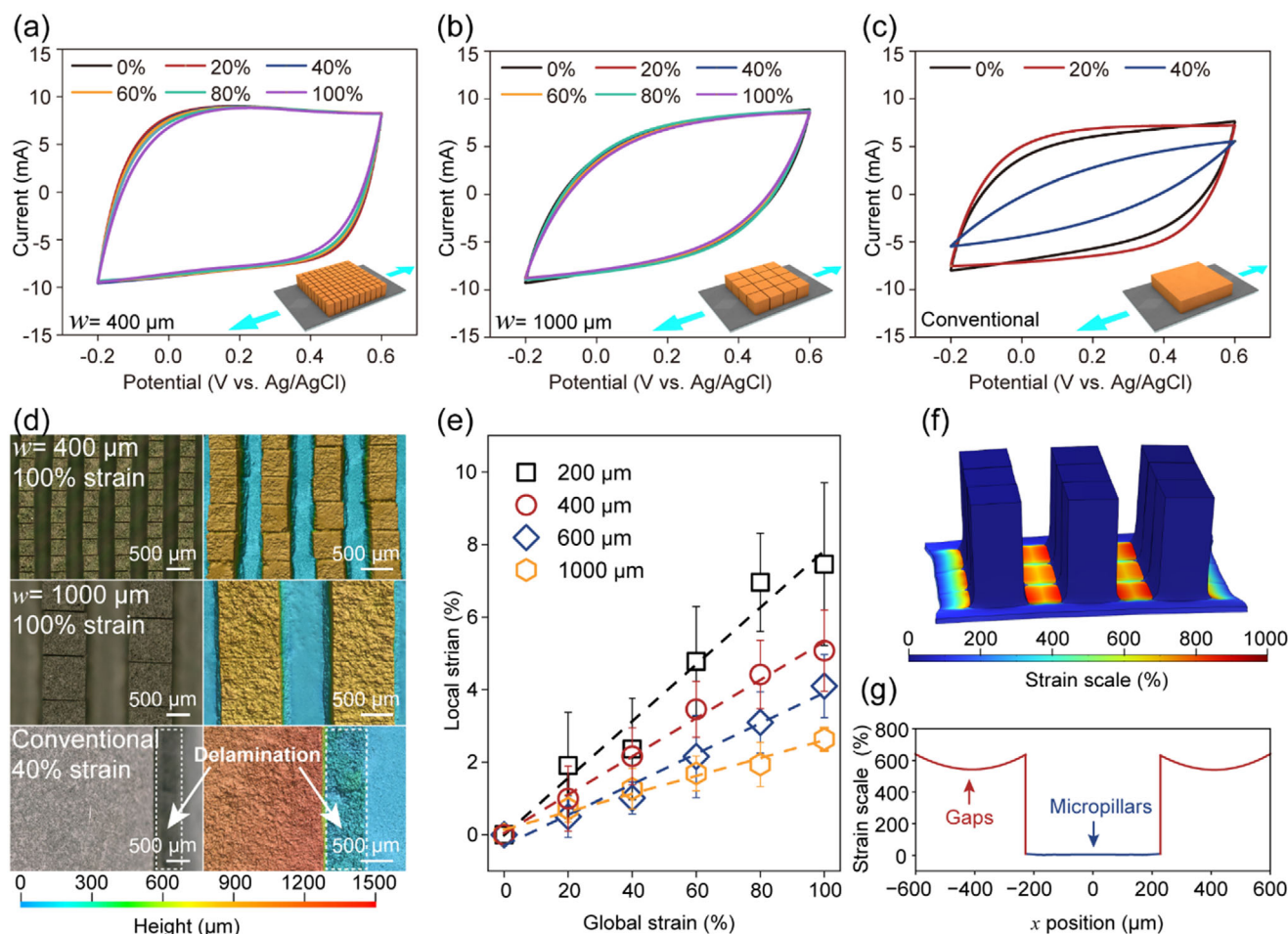
ADVANCED
FUNCTIONAL
MATERIALS

www.afm-journal.de

Figure 2. Fabrication, structural characterizations, and electrochemical performance of the bioinspired 3D electrodes. a) Schematic illustration of the fabrication procedures. b) Top-view (up) and side-view (bottom) optical microscopy images of the pillar array. c) SEM image showing the porous scaffold of individual pillars. d) SEM images revealing the microstructure of an individual pillar after loading the active material. e) Cyclic voltammetry (CV) curves at 20 mV s^{-1} for electrodes with pillar widths (w) ranging from 200 to 2500 µm. f) Areal capacitance versus pillar width (w) at varying scan rates. Data represent mean ± s.d. ($n = 5$). g) CV curves at 20 mV s^{-1} for the electrode with pillar thicknesses (h) ranging from 350 to 1100 µm. h) Areal capacitance versus pillar thickness (h) at varying scan rates. Data represent mean ± s.d. ($n = 5$).

the areal capacitance increases with thickness up to 900 µm, driven by higher loading of the active material. However, the capacitance begins to decline at a thickness of 1100 µm due to diffusion limitations.[57,58] This trend persists across various scan rates, as illustrated in Figure S11 (Supporting Information).

Overall, the optimal electrode design features pillars of a width of 400 µm and a thickness of 900 µm, which overcomes the critical thickness limits (≤300 µm) for conventional electrodes.[59] These electrodes demonstrate high areal capacitance of 443, 382, and 285 mF cm^{-2} at scan rates of 5, 20, and 50 mV s^{-1}, respectively.

The balance between areal capacitance and rate capability is critical for supercapacitors. In this context, the mass loading of active material in the electrode is controlled by the electrode-

position cycle number, which consequently affects their electrochemical behavior. As illustrated in Figures S12 and S13 (Supporting Information), the capacitance increases with cycles up to 200. Beyond this point, additional cycles result in only marginal improvements in capacitance at low scan rates below 50 mV s^{-1} while significantly degrading rate performance. This trend is consistent across electrodes with varying pillar dimensions, establishing 200 cycles as an optimal condition for balanced performance. With optimized electrodeposition cycles, the mass loading of the PEDOT nanocomposite is calculated to be 10 mg cm^{-2} (Figure S14, Supporting Information), which achieves a practical level of mass loading for real-world applications.[36]

**ADVANCED
SCIENCE NEWS**

www.advancedsciencenews.com

**ADVANCED
FUNCTIONAL
MATERIALS**

www.afm-journal.de

Figure 3. Bioarmor-inspired 3D electrodes during stretching. a) CV curves of electrodes with 400 μm-wide pillars across a strain range from 0% to 100%. b) CV curves of electrodes with 1000 μm-wide pillars across a strain range from 0% to 100%. c) CV curves of electrodes without the pillar design under tensile strain. d) Optical images (left) and the corresponding surface topographic images (right) of stretched electrodes. e) Local strain of pillars with varying widths with respect to the applied global strain. Data represent mean ± s.d. ($n = 7$). f) Strain distribution of electrodes with 400 μm-wide pillars at 100% strain derived from finite element simulation. g) Strain profile along the central line cut of the pillars.
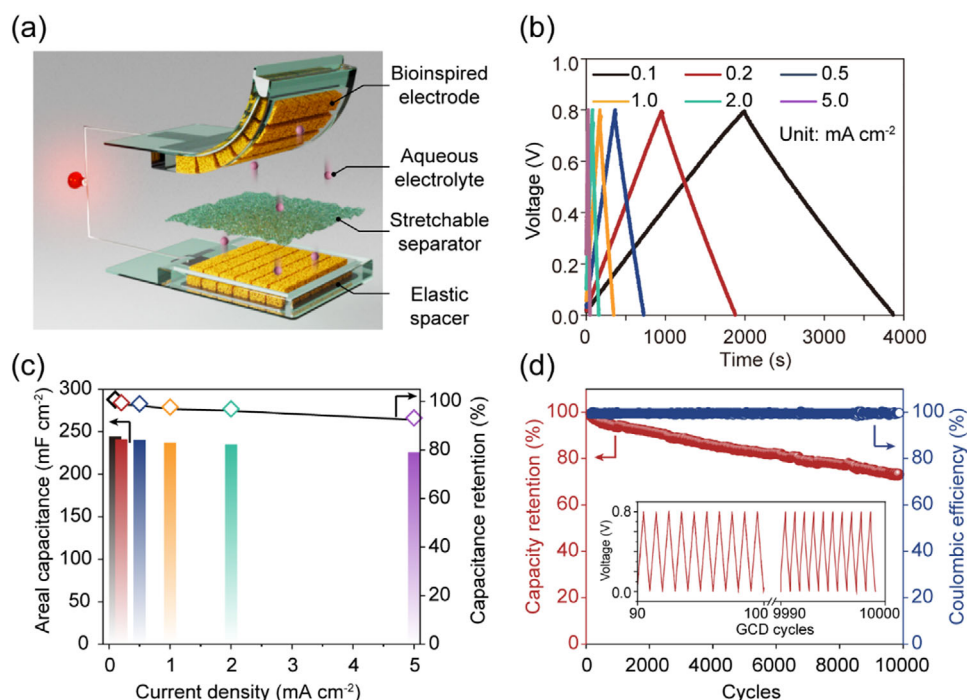
The mechanical stretchability of the bioarmor-inspired electrodes is thoroughly explored. As shown in **Figure 3a**, CV curves of the optimal electrodes with 400 μm-wide pillars remain nearly rectangular and overlapping across tensile strains ranging from 0% to 100%, indicating strain-insensitive behavior. The areal capacitance is 373.3 mF cm^{-2} in the relaxed state and 360.5 mF cm^{-2} at 100% strain, corresponding to a 96.6% retention (Figure S15, Supporting Information). Furthermore, the electrode exhibits excellent cyclic durability, retaining 76.7% of its initial capacitance after 1000 stretching cycles (refer to Figure S16, Supporting Information). This gradual attenuation in performance is attributed to increased ohmic loss stemming from mechanical fatigue within the electrode structure during repeated deformation (refer to Figure S17, Supporting Information).

The structural integrity of the pillar-based electrodes under mechanical strain is demonstrated in Figure 3d. Optical images reveal that electrodes with 400 μm-wide pillars remain largely intact at 100% strain. This robustness is further confirmed by SEM imaging (Figure S18, Supporting Information), which shows no observable delamination or cracking. We attribute this stability

to an effective strain-redistribution mechanism: applied tension primarily elongates the gaps between adjacent pillars, while the pillars themselves undergo minimal deformation. A comparable level of stability is observed in electrodes featuring 1000 μm-wide pillars, which shows 98.0% capacitance retention under 100% strain (see Figure 3b and Figure S15, Supporting Information). In stark contrast, conventional rigid electrode layers without this design suffer severe distortion in CV curves during stretching, as depicted in Figure 3c. These electrodes retain only 60.0% of their capacitance at 40% strain and ultimately fail at further increased deformation. This failure is characterized by structural damage, specifically the detachment of the electrode layer from the current collector at 40% strain (Figure 3d). This delamination issue is further corroborated by SEM imaging, as shown in Figure S18 (Supporting Information).

The exceptional structural integrity of the bioarmor-like electrodes stems from their capability to modify strain distribution. Although the porous scaffold and current collector share similar mechanical moduli (refer to Figure S19, Supporting Information), the scaffold's sixfold greater thickness confers significantly

**ADVANCED
SCIENCE NEWS**

www.advancedsciencenews.com

**ADVANCED
FUNCTIONAL
MATERIALS**

www.afm-journal.de

Figure 4. Electrochemical performance of symmetric supercapacitors using bioinspired 3D electrodes. a) Schematic illustration of a supercapacitor cell. b) GCD profiles at different current densities ranging from 0.1 to 5.0 mA cm^{-2}. c) Areal capacitance versus current density. d) Long-term GCD cycles at a current density of 1.0 mA cm^{-2}.

higher tensile stiffness to the pillars. Consequently, the applied tension primarily localizes in the softer current collector, sparing the pillars from substantial deformation. Local strain analysis confirms minimal pillar elongation under 100% global strain: ≈5.1% for 400 µm-wide pillars and ≈2.6% for 1000 µm-wide pillars (see Figure 3e). In contrast, conventional electrodes lacking this design suffer interfacial delamination at 40% strain, as illustrated in Figure 3d.

Finite element analysis (FEA) simulations have been conducted to explore the mechanical behavior of the bioarmor-inspired electrodes. Figure 3f displays the strain distribution in electrodes featuring 400 µm-wide pillars subjected to 100% global strain. The corresponding strain profile along the central axis is summarized in Figure 3g. The simulation reveals a significant strain redistribution effect: the gaps between the pillars experience considerable expansion, exceeding 540% strain, while the pillars themselves undergo minimal deformation, with strain levels below 5%. Additional simulation results at various global strains can be found in Figure S20 (Supporting Information). The predicted local strain in the pillars is documented across different global strains, as summarized in Figure S21 (Supporting Information). This local strain increases progressively with stretching, reaching 4.4% at 100% global strain, which aligns closely with experimental data. These results suggest that the bioarmor-like design effectively isolates strains, shielding the pillar scaffold from substantial deformation even under significant tensile loads.

The overall mechanical characteristics of bioarmor-inspired electrodes are preserved after loading the active materials. The deposition of the PEDOT nanocomposite further strengthens the pillars, enhancing their stiffness in contrast to the substrate and

improving strain isolation (see Figure S22, Supporting Information). Specifically, the elongation of the 400 µm-wide pillars is lowered to ≈3.9% under 100% global strain, as shown in Figure S23 (Supporting Information). In comparison, a conventional electrode experiences severe fracture at just 20% global strain. These findings demonstrate that the bioarmor-inspired architecture, with its strain redistribution capability, serves as a robust electrode platform for stretchable supercapacitors.

The prevailing strategy for stretchable devices involves incorporating rigid electronic components into soft substrates, which are interconnected by conductive wiring for strain management. Our bioarmor-inspired electrode design advances this approach by replacing the ubiquitous, fragile wiring of island-bridge designs with a more robust and efficient architecture. Here, a densely packed array of rigid pillars is fabricated directly onto a seamless, soft current collector using laser ablation. This integration not only simplifies the design but also maximizes the effective surface area for active material, overcoming a major constraint in achieving high density.[37] Additionally, the pillars form a homogeneous, thermally welded interface with the collector, guaranteeing mechanical robustness. This inherent durability is achieved without the need for further strain-engineering modifications to the substrate itself.[60]

Figure 4a depicts the architecture of a symmetric supercapacitor cell, consisting of two identical armor-like electrodes and a soft separator within an elastomeric package. The separator in the form of an elastomer microsponge film is prepared via a sacrificial template-based approach using salicylic acid microrods as a hard template. This separator can easily sustain tensile strains up to 100%, as shown in Figure S24 (Supporting Information).

**ADVANCED
SCIENCE NEWS**

www.advancedsciencenews.com

**ADVANCED
FUNCTIONAL
MATERIALS**

www.afm-journal.de

For the electrolyte, a 1 M LiCl aqueous solution is employed. The nonflammable nature of aqueous electrolytes provides a critical safety advantage for skin-attached wearable electronics compared to organic electrolytes.[18,61] After electrolyte infusion, the separator achieves a stable ionic conductivity of ≈0.12 S cm^{-1}, which remains nearly constant under strains from 0% to 100% (see Figure S25, Supporting Information). During final cell assembly, an SEBS-based elastomer spacer is introduced to accommodate the ultrathick electrodes and guarantee a robust seal within the SEBS package. The inherent biocompatibility of SEBS ensures the final device is suitable for comfortable, long-term skin attachment.[62,63]

In Figure 4b, the GCD curves display nearly symmetric triangular shapes across current densities from 0.1 to 5.0 mA cm^{-2}, with Coulombic efficiencies approaching ≈100%, which indicates rapid ion adsorption/desorption kinetics. The device achieves an areal capacitance of 244.5 mF cm^{-2} at 0.1 mA cm^{-2} and 226.0 mF cm^{-2} at 5.0 mA cm^{-2} (refer to Figure 4c), demonstrating excellent rate capability with 92.4% capacitance retention despite a 50-fold increase in current density. This performance translates into an outstanding energy density of 21.7 µWh cm^{-2} at a power density of 41 µW cm^{-2} and 20.1 µWh cm^{-2} energy density even at a high power density of 2904 µW cm^{-2}. Moreover, the CV curves maintain a nearly rectangular shape at low scan rates and then gradually distort as the rate increases (see Figure S26, Supporting Information). As summarized in Table S1 (Supporting Information), the critical performance metrics of our device, including mass loading, areal capacitance, and capacitance retention under strain, surpass those of most PEDOT-based flexible/stretchable supercapacitors in the literature. The combination of attributes is essential for stretchable and wearable applications where the footprint area is constrained. On the other hand, the gravimetric and volumetric capacitances are less competitive, a known trade-off for thicker, less densely packed 3D electrodes.[31]

The electrochemical cycling performance is assessed through GCD measurements at 1.0 mA cm^{-2}, as shown in Figure 4d. Although there is a gradual increase in IR drop, the GCD profiles remain nearly identical between the 90th–100th and 9 990th–10 000th cycles, with 72.7% capacitance retention after 10 000 cycles. The device maintains a Coulombic efficiency exceeding 99% throughout cycling, underscoring its dominance of capacitive charge storage over parasitic reactions. SEM analysis presented in Figure S27 (Supporting Information) depicts well-preserved structures of electrodes after long-term cycling, suggesting the electrode degradation as a secondary effect. The capacitance decay is primarily attributed to significant electrolyte evaporation over the extended cycling period (>1 month). Remarkably, upon replenishing the electrolyte, 88.4% of the initial capacitance is restored, accompanied by a reduced IR drop (Figure S28, Supporting Information). These results highlight the need for improved hermetic sealing capability of the cell package to enhance long-term device stability.[64]
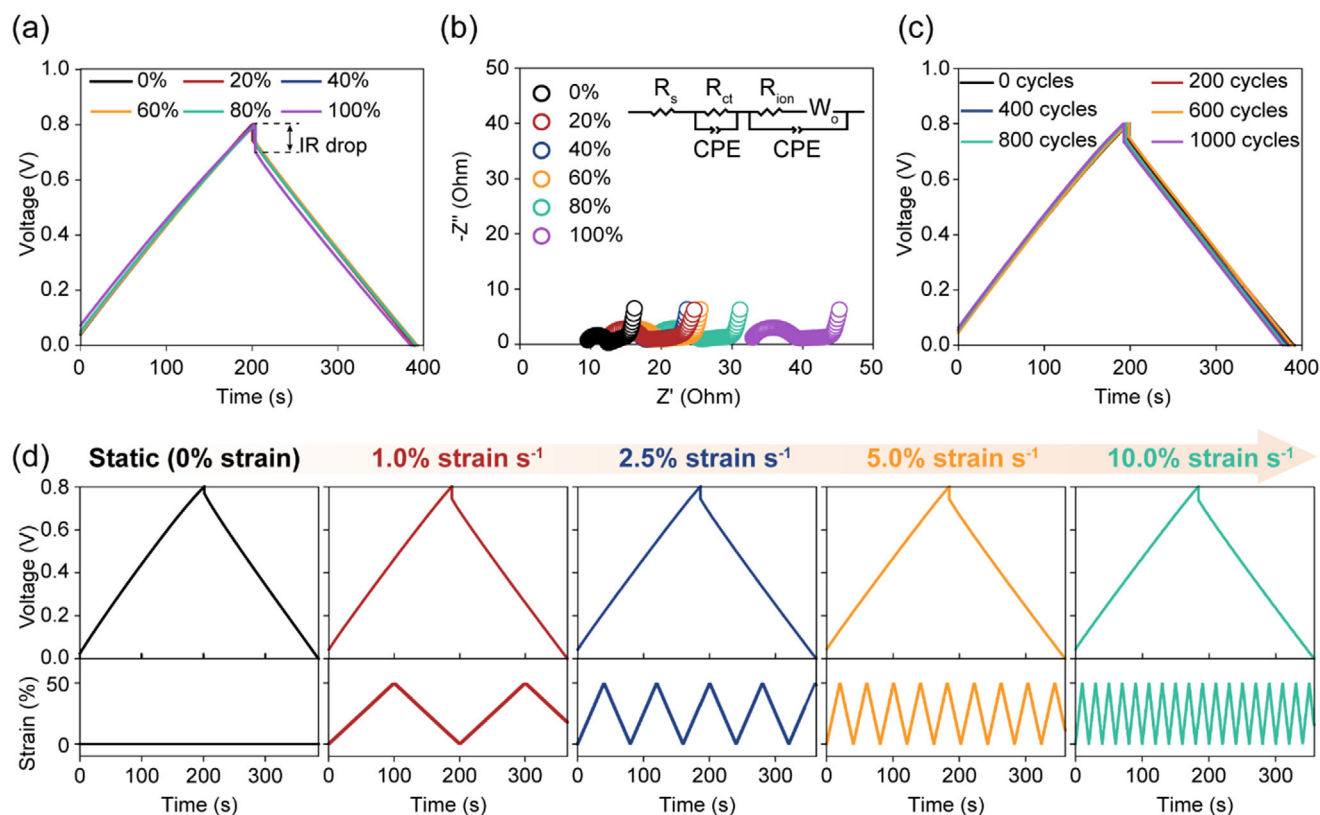
As a skin-attachable power source, the environmental stability of the stretchable supercapacitor is critical for practical wearable applications. To evaluate its robustness, we systematically assessed the electrochemical performance under varying humidity and temperature conditions mimicking real-world wearable environments. As shown in Figure S29 (Supporting Information),

the device retains its characteristic triangular GCD profiles without degradation, demonstrating insensitivity to ambient humidity or temperature fluctuations. These findings highlight the supercapacitor's reliability as a durable energy source for wearable electronics.

The mechanical deformability of the supercapacitor cell is systematically investigated. GCD curves maintain near-ideal triangular shapes across tensile strains from 0% to 100%, with only minor reductions in charge/discharge duration at higher strains (see **Figure 5a**). Areal capacitance retains 95.5% of its initial value at 100% strain despite a minor increase in the IR drop (see Figure S30, Supporting Information). Electrochemical impedance spectroscopy (EIS) analysis in Figure 5b elucidates strain effects on the cell. Nyquist plots are decomposed into circuit elements: an ohmic cell resistance (R_s), a depressed semicircle related to charge transfer resistance (R_{ct}), a slope reflecting ionic resistance (R_{ion}), and a Warburg diffusion element (W_o) (see Table S2, Supporting Information).[36] R_s rises from 9.4 to 32.5 Ω during stretching, attributed to the elongatation of the current collectors. R_{ct} and R_{ion}, however, show minor variations, underscoring intact ion transport pathways enabled by the bioarmor-inspired electrode design. In addition, the supercapacitor exhibits exceptional mechanical durability to endure 1000 stretching cycles to 50% strain (refer to Figure 5c). GCD curves exhibit negligible degradation, with 97.5% capacitance retention after tensile fatigue testing (Figure S31, Supporting Information). Post-cycling EIS analysis reveals only marginal increases in R_s, R_{ct}, and R_{ion}, consistent with the stable electrochemical behavior (refer to Figure S32 and Table S3, Supporting Information). Given that human skin typically experiences strains below 50% during daily activities like walking or running.[4,8] This robust durability ensures the supercapacitor's reliable operation in wearable application settings.

Beyond static deformation, practical applications require energy storage devices to withstand dynamic mechanical stresses.[65–67] To evaluate performance under such conditions, we characterized our supercapacitors under repeated stretching at varying strain rates. As shown in Figure 5d, the GCD profiles consistently exhibit ideal symmetric triangular shapes across strain rates from 0 to 10.0% s^{-1} in a 50% strain range. The corresponding capacitance remains virtually unchanged, demonstrating durable energy storage capability despite mechanical perturbations (see Figure S33, Supporting Information). CV curves during dynamic stretching further support this stability, as they almost completely overlap, with only minor voltage fluctuations emerging at the highest strain rate (refer to Figure S34, Supporting Information). To assess performance under extreme conditions, we extend the evaluation to a higher strain range from 50% to 100%. In this regime, the GCD curves exhibit clear voltage fluctuations that correlate directly with the strain cycles, as shown in Figure S35 (Supporting Information). Despite this, the discharge branches of five consecutive GCD cycles remain highly consistent, indicating predictable electrochemical responses to dynamic strains (Figure S36, Supporting Information). The overall capacitance experiences only a slight reduction, retaining 83% of its initial value accordingly. Collectively, these findings demonstrate the supercapacitor's extremely stable electrochemical performance regardless of external mechanical loads and impacts.

The exceptional performance of our stretchable supercapacitors underscores the versatility of the bioinspired electrode

**ADVANCED
SCIENCE NEWS**

www.advancedsciencenews.com

**ADVANCED
FUNCTIONAL
MATERIALS**

www.afm-journal.de

Figure 5. Electrochemical performance of the supercapacitor under tensile deformations. a) GCD curves at different strains. b) EIS spectra of the supercapacitor cell at different strains. The inset shows the corresponding equivalent circuit model. c) GCD curves after different stretch-relaxation cycles up to 50% strain. d) GCD curves and the in situ strain profiles of the supercapacitor at static and dynamic stretching-releasing modes.
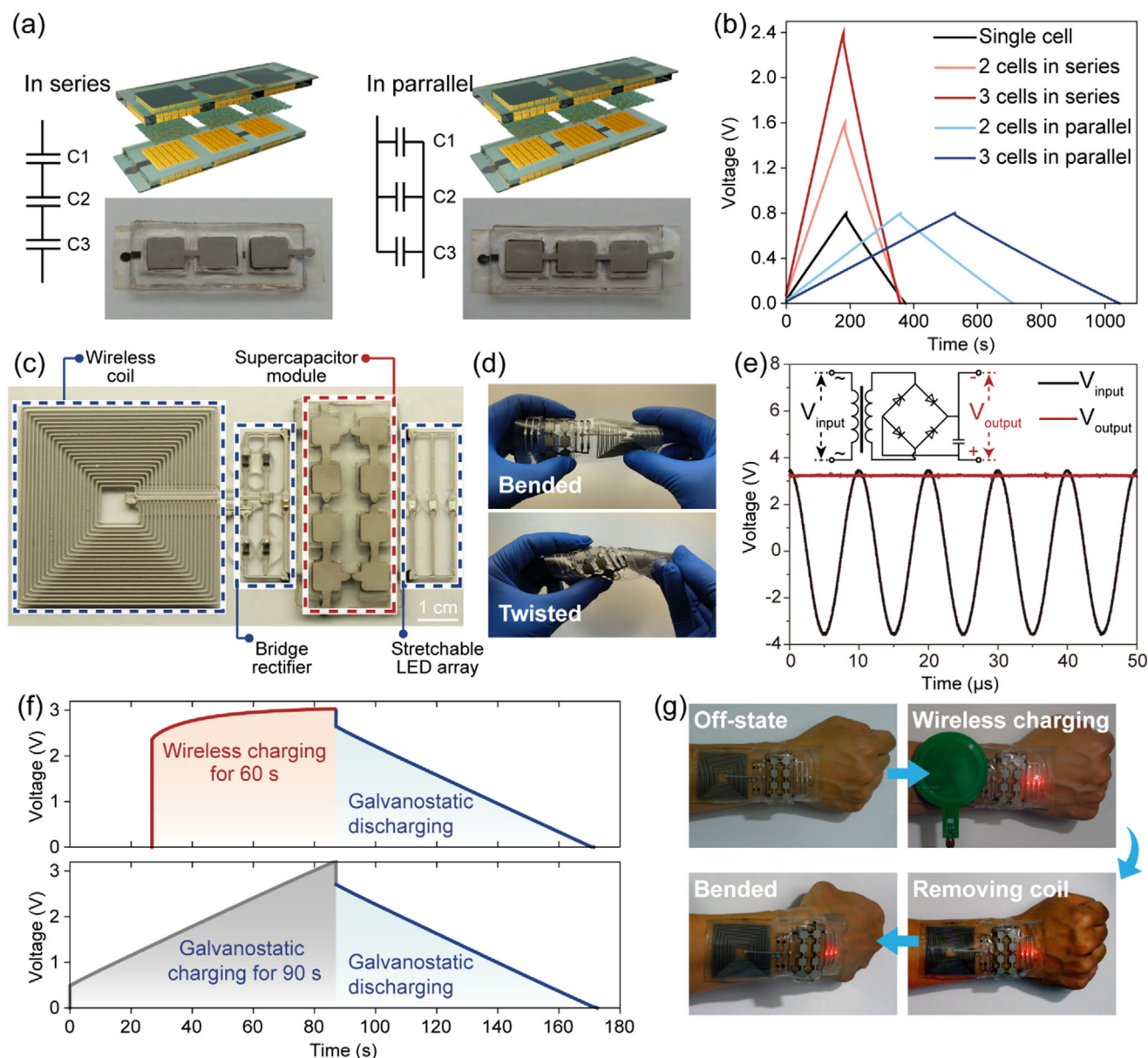
architecture. Crucially, the 3D porous scaffold is not limited to a single electrochemistry but can be adapted to various active materials for energy storage. To showcase this general applicability, we create symmetric supercapacitors using polyaniline (PANI) as an alternative active material. These devices deliver an exceptional areal capacitance of 1182.5 mF cm^{-2} and an 89.7% capacitance retention even at 100% strain. These performance metrics compete favorably with, or even surpass, other recently reported stretchable PANI-based supercapacitors (Figures S37 and S38, Table S4, Supporting Information). This successful proof-of-concept demonstration confirms that our bioarmor-like design strategy is a robust and versatile platform, paving the way for developing a diverse range of high-performance, stretchable energy storage devices.

Stretchable supercapacitors with high capacitance are critical for powering deformable forms of electronic devices. It is straightforward to integrate multiple supercapacitors in series or parallel configurations, allowing adjustable operating voltage and capacitance to meet practical application-specific demands (see **Figure 6a**). GCD measurements are employed to evaluate the energy storage performance of these modular systems. As shown in Figure 6b, when operated at a constant current, the charge/discharge duration increases linearly with the number of parallel-connected cells, proportionally enhancing the total capacitance. Similarly, the operating voltage scales with the number of series-connected cells, significantly boosting the power density

of the module. This modular design facilitates convenient tuning of energy and power densities, positioning the system as a promising solution for wearable electronics.

For skin-mounted applications, wireless charging is essential for electronic systems to avoid vulnerable and unreliable physical connections to external power supplies.[68] To this end, a prototype electronic system is created to realize wireless charging for on-skin wearable usage. As shown in Figure 6c, the entire electronic system is comprised of a wireless coil, a bridge rectifier, a supercapacitor module, and a stretchable LED array. The supercapacitor module consists of eight cells arranged in a hybrid configuration: four cells are connected in series, and this unit is placed in parallel with a second, identical series unit. This configuration delivers the required capacitance and operating voltage to illuminate the LED array. Taking advantage of the versatility of materials and designs (see details of experimental section), these compliant components for an electronic system can be monolithically integrated on an elastomer substrate, which ensures excellent mechanical deformability, including bending and twisting (see Figure 6d). The operation of the wireless charging process is illustrated in Figure 6e. The transmitter coil couples the electromagnetic flux from a primary coil, and the bridge rectifier, composed of a Schottky diode bridge and a smoothing capacitor, provides rectification (refer to the inset in Figure 6e). When a 7.0 V alternating voltage at 100 kHz is applied to the transmitter coil, the circuit generates a stable 3.2 V output that

**ADVANCED
SCIENCE NEWS**

www.advancedsciencenews.com

**ADVANCED
FUNCTIONAL
MATERIALS**

www.afm-journal.de

Figure 6. Integration of the supercapacitor module into wearable electronic systems. a) Supercapacitor modules with three cells connected in series (left) and in parallel (right). b) GCD curves at 1.0 mA cm^{-2} acquired from supercapacitor modules. c) Optical images of the self-powering electronic system that consists of a wireless coil, a bridge rectifier, a supercapacitor module, and a stretchable LED array. d) The electronic system under bending and twisting manipulations. e) Input voltage of the external charging coil and output voltage of the wireless charging system as a function of time. The inset shows the circuit diagram of the wireless charging system. f) Voltage profiles of the supercapacitor module subjected to wireless charging/galvanostatic discharging (top) and GCD (bottom). The current of GCD is set to 1 mA. g) Optical images showing the operation of the entire system attached to the back of the hand.

is well suited to charge the supercapacitor module. The supercapacitor voltage rapidly rises to 2.4 V upon charging initiation and reaches ≈3.0 V within 60 s, as shown in Figure 6f. Subsequent discharge at a constant current matches the duration of conventionally charged modules, confirming comparable energy storage performance. Furthermore, the entire system can be easily applied to the back of the hand, achieving conformal integration to the skin (see Figure 6g). The LED array is initially inactive due to the lack of a power supply. As the external transmitter coil

approaches to the system, the energy harvested from electromagnetic radiation effectively charges the supercapacitor module and lights up the LED array simultaneously. When the external coil is removed, the supercapacitor module sustains the LED illumination. Due to the excellent mechanical deformability of the entire system, the LED array maintains stable brightness during wrist movements. These results demonstrate the practical suitability of the supercapacitors to function as deformable energy supplies within stretchable electronic systems.

**ADVANCED
SCIENCE NEWS**

www.advancedsciencenews.com

**ADVANCED
FUNCTIONAL
MATERIALS**

www.afm-journal.de

3. Conclusion

In this study, we propose a 3D electrode design for wearable supercapacitors that effectively combines superior areal capacitance and high stretchability. Drawing inspiration from the armadillo's dermal armor, a densely packed array of stiff porous pillars is mounted on a soft nanocomposite current collector, successfully decoupling electrochemical performance and applied tensile forces. The porous pillars, optimized to dimensions of 900 μm in thickness and 400 μm in width, facilitate a high-mass-loading of 10 mg cm^{-2}, surpassing the practical limit of traditional electrodes. By utilizing PEDOT as the active material, the assembled symmetric supercapacitors exhibit an impressive areal capacitance of 244.5 mF cm^{-2}, a long lifespan of 10000 charge-discharge cycles, and high rate performance. Additionally, the stiffness contrast between pillars and the current collector allows for significant strain isolation in these 3D electrodes during deformation. Under a global strain of 100%, the actual strain experienced by the individual pillars is dramatically reduced to just 5.1%, thereby preserving their electrochemical integrity. The corresponding supercapacitors can withstand tensile strains of up to 100% while retaining > 95.5% of their initial capacitance. Moreover, the supercapacitors are capable of handling dynamic strains at varying rates, demonstrating resilience against unexpected mechanical loads and impacts. We have successfully created a skin-attached wearable electronic system using a supercapacitor module for energy storage and supply, coupled with wireless charging components to achieve extended operation. The versatility of the electrode is further validated by fabricating supercapacitor cells utilizing PANI as the active material, achieving an exceptional areal capacitance of 1182.5 mF cm^{-2} and high capacitance retention at 100% strain. Overall, this bioarmor-inspired electrode design presented here resolves the inherent trade-off between electrochemical performance and mechanical deformability in stretchable energy storage devices.

4. Experimental Section

Chemicals and Reagents: Soft SEBS elastomer (Tuftec H1221, 12% polystyrene) was provided by Asahi Kasei, while rigid SEBS elastomer (Kraton G1652, 29% polystyrene) was obtained from Kraton Inc. Hydrocarbon resin (Cleartack W-85) was supplied by Cary Valley. Multiwall carbon nanotubes (MWCNTs, XFM07, length ≈50 μm) were purchased from Nanjing XFNANO Materials Tech Co., Ltd. Salicylic acid (99.0%), 3,4-ethylenedioxythiophene (99.0%), poly(sodium 4-stryrenesulfonate) (Mw ≈70 000), aniline (99.5%), sodium sulfate (99.0%), lithium chloride (99.0%), and gum xanthan (USP grade) were sourced from Shanghai Aladdin Co., Ltd. All solvents were purchased from Sinopharm Co., Ltd, including toluene, isopropanol, trichloromethane, xylene, and ethanol. Deionized water (resistivity: 18.2 MΩ·cm) was used for all aqueous solutions. Silver nanowires (AgNWs) were synthesized via a modified polyol reduction method.[69] Salicylic acid microrods were prepared through an antisolvent crystallization technique.[70]

Fabrication of Stretchable Current Collectors: A mixture of soft SEBS solution (20 wt.% in toluene), a hydrocarbon resin solution (20 wt.% in toluene), and multi-walled carbon nanotubes (MWCNTs) at a 40:10:5 weight ratio was homogenized by bead milling at 2000 rpm for 2 h. This mixture was blade-coated onto a non-sticky glass wafer treated with octadecyltrichlorosilane. After natural drying, silver nanowires dispersed in isopropanol were spray-deposited at ≈2 mg cm^{-2}, forming a bilayer nanocomposite of ≈60 μm in total thickness. The nanocomposite was patterned into desired shapes via selective laser ablation using a 1064 nm

benchtop laser marking system from Dayin Technology Co., Ltd. A soft SEBS solution (20 wt.% in toluene) was drop-cast and dried naturally. The resulting ≈150 μm-thick current collector was peeled off the glass wafer for further use.

Fabrication of Bioarmor-Inspired 3D Electrodes: A composite film of soft SEBS, hydrocarbon resin, and MWCNTs was first prepared on a non-sticky glass wafer. Subsequently, a mixture containing rigid SEBS solution (20 wt.% in toluene), MWCNTs, and salicylic acid microrods at a weight ratio of 85:15:200 was homogenized and cast onto this film. After natural drying, the entire composite was patterned into a pillar array by selective laser ablation. To provide mechanical support during handling, a poly(vinyl alcohol) (PVA) solution (10 wt.% in water) was drop-cast and vacuum-dried at 80 °C for 20 min. The stiffened pillar array was then peeled off from the glass wafer. Prior to bonding, the surface of the current collector was temporarily softened by spraying with xylene. The pillar array was attached to the softened current collector under 60 °C and 1 kPa pressure for 5 min using a vacuum thermal laminator. The sacrificial PVA support was then dissolved by rinsing in hot water.

Poly(3,4-ethylenedioxythiophene) (PEDOT) was electrodeposited onto the porous conductive scaffold via cyclic voltammetry, carried out within −0.5 and 1.0 V versus Ag/AgCl reference electrode at a scan rate of 20 mV s^{-1}. The electrolyte was prepared by dissolving 0.7 g poly(sodium 4-stryrenesulfonate), 1.42 g sodium sulfate, and 0.28 g 3,4-ethylenedioxythiophene monomer in 100 mL of water. MWCNTs (0.1 g) were then dispersed into this solution via tip sonication set at 200 W for 20 min To enhance electrolyte penetration, the electrode underwent oxygen plasma treatment for 5 min before electrodeposition. The active material loading was adjusted by varying the number of CV cycles. Finally, the electrode was rinsed sequentially with ethanol and water three times. Polyaniline was also electrodeposited onto the porous pillars using cyclic voltammetry. The electrolyte was prepared by dissolving 0.1 M aniline and 0.25 M H$_2$SO$_4$ in deionized water. MWCNTs were dispersed into this electrolyte using 1 wt.% sodium dodecylbenzenesulfonate under tip sonication at a concentration of 1 mg mL^{-1}. The electrodeposition was performed at 0.85 V versus Ag/AgCl reference electrode for 1800 s.

Fabrication of Stretchable Supercapacitors: The stretchable supercapacitor adopted a standard sandwich configuration comprising two stretchable electrodes and a separator (refer to Figure 4a). The 200 μm-thick stretchable separator was fabricated using a sacrificial template method. Specifically, a homogeneous mixture of soft SEBS solution (20 wt.% in toluene) and salicylic acid microrods at 1:3 weight ratio was cast onto a glass wafer and dried naturally. Subsequent washing with ethanol removed the salicylic acid microrods, yielding the porous separator. For cell assembly, the electrodes and separator were stacked sequentially. An elastic spacer composed of soft SEBS and hydrocarbon resin mixed at 1:1 weight ratio was introduced to match the height of the electrode pillars. The cell was infused with an aqueous 1 M LiCl electrolyte. Finally, robust sealing was achieved by thermally bonding the elastic spacer and elastomer packaging under elevated temperature. The PANI-based supercapacitors were fabricated following the same experimental procedures with 1 M H$_2$SO$_4$ solution as electrolyte.

Device System Integration: The fully integrated electronic system comprised three primary device components: a supercapacitor module, a wireless charging circuit, and a stretchable LED array. The supercapacitor module was created on the elastomer substrate consisting of eight cells arranged as two parallel units, each containing four cells connected in series. A liquid metal ink, formulated following recently reported method,[71] was printed to form the circuit pattern, including antenna, interconnects, and contact pads. Discrete chip components, specifically Schottky diodes (1206, Risym SS34), capacitors (0805, 1 μF), and LEDs (1206), were then mounted on the contact pads. An acrylic resin (LOCTITE AA3944) was used to secure these chips in place. The fully assembled system was conformally attached to the forearm for on-body testing using a silicone gel adhesive (Silbione RT gels, Elkem).

Materials Characterization: The resistance was measured under a four-probe configuration using a Keithley 2110 sourcemeter. The tensile strain was applied using customized motorized uniaxial stages. Microstructure characterizations were obtained using a Zeiss Ultra 55 field-emission

**ADVANCED
SCIENCE NEWS**

www.advancedsciencenews.com

**ADVANCED
FUNCTIONAL
MATERIALS**

www.afm-journal.de

scanning electron microscope equipped with an energy dispersive X-ray spectroscopy detector. Surface topography was acquired with a Keyence VK-X1000 confocal laser scanning microscope. Mechanical properties were measured using a Shimadzu AGS-X universal testing machine. Optical images were captured with a Fujifilm X-T10 camera.

Electrochemical Measurements: The electrochemical characteristics and electrochemical impedance spectroscopy (EIS) analysis were carried out with a CHI 660E electrochemical workstation. Electrochemical stability of the current collector was assessed using linear sweep voltammetry in a three-electrode configuration, with the carbon rod counter electrode and Ag/AgCl reference electrode. Cyclic voltammetry (CV) and galvanostatic charge-discharge (GCD) measurements were performed to assess the electrochemical performance of the stretchable electrodes and supercapacitor cells. The stretchable electrode served as the working electrode, while the stainless steel foam coated with activated carbon (Kurary YP-50F) was employed as the counter electrode, and Ag/AgCl electrode as the reference electrode. The energy storage performance of supercapacitor cells was evaluated by CV and GCD measurements using a LAND CT2001A battery measurement system. After a 10-min stabilization period, EIS was performed at open circuit voltage, applying a 5-mV perturbation across a frequency range from 100 kHz to 0.1 Hz. The areal capacitance was calculated based on the footprint of the pillar array. For environmental stability tests, temperature was controlled using an oven, and relative humidity was regulated within sealed vessels containing various saturated salt solutions. Humidity levels were quantified using a CENTER 314 digital thermohygrometer.

Finite Element Analysis: Finite element analysis was performed using Comsol Multiphysics software to simulate stress distributions across the electrode under strain. The hyperelastic behavior of the material components, including the soft SEBS elastomer, bilayer conductive nanocomposite, and stiff pillars, was modelled using the Ogden constitutive law. Material parameters were derived by fitting experimental stress-strain curves. A refined mesh was applied during simulation to ensure computational accuracy.

Supporting Information

Supporting Information is available from the Wiley Online Library or from the author.

Acknowledgements

Conflict of Interest

The authors declare no conflict of interest.

Data Availability Statement

The data that support the findings of this study are available from the corresponding author upon reasonable request.

Keywords

[1] A. Vázquez-Guardado, Y. Yang, J. A. Rogers, *Nat. Sci. Rev.* **2022**, *9*, nwac016.
[2] Y. Jiang, S. Ji, J. Sun, J. Huang, Y. Li, G. Zou, T. Salim, C. Wang, W. Li, H. Jin, J. Xu, S. Wang, T. Lei, X. Yan, W. Y. Xian Peh, S.-C. Yen, Z. Liu, M. Yu, H. Zhao, Z. Lu, G. Li, H. Gao, Z. Liu, Z. Bao, X. Chen, *Nature* **2023**, *614*, 456.
[3] J. C. Yang, J. Mun, S. Y. Kwon, S. Park, Z. Bao, S. Park, *Adv. Mater.* **2019**, *31*, 1904765.
[4] C. Zhao, J. Park, S. E. Root, Z. Bao, *Nat. Rev. Bioeng.* **2024**, *2*, 671.
[5] S. Liu, Y. Rao, H. Jang, P. Tan, N. Lu, *Matter* **2022**, *5*, 1104.
[6] J. A. Rogers, T. Someya, Y. Huang, *Science* **2010**, *327*, 1603.
[7] J. Li, J. Zhao, J. A. Rogers, *Acc. Chem. Res.* **2019**, *52*, 53.
[8] D. G. Mackanic, T.-H. Chang, Z. Huang, Y. Cui, Z. Bao, *Chem. Soc. Rev.* **2020**, *49*, 4466.
[9] J. Xu, T. Tat, J. Yin, D. Ngo, X. Zhao, X. Wan, Z. Che, K. Chen, L. Harris, J. Chen, *Matter* **2023**, *6*, 2235.
[10] C. Bai, S. Li, K. Ji, M. Wang, D. Kong, *Energy Materials* **2023**, *3*, 300041.
[11] J. He, L. Cao, J. Cui, G. Fu, R. Jiang, X. Xu, C. Guan, *Adv. Mater.* **2024**, *36*, 2306090.
[12] Y. Huang, M. Zhong, F. Shi, X. Liu, Z. Tang, Y. Wang, Y. Huang, X. Xie, C. Zhi, *Angew. Chem. Int. Ed.* **2017**, *56*, 9141.
[13] M. Hu, J. Wang, J. Liu, P. Wang, Y. Feng, H. Wang, N. Nie, Y. Wang, Y. Huang, *Energy Storage Mater.* **2019**, *21*, 174.
[14] Z. Cao, Y.-B. Zhu, K. Chen, Q. Wang, Y. Li, X. Xing, J. Ru, L.-G. Meng, J. Shu, N. Shpigel, L.-F. Chen, *Adv. Mater.* **2024**, *36*, 2401271.
[15] J. Han, B. Xu, C. Fang, J. Wei, Z. Li, X. Liu, Y. Yang, Q. Wang, J. Zhang, *Adv. Sci.* **2025**, *12*, 2500835.
[16] J. Li, P. Yang, X. Li, C. Jiang, J. Yun, W. Yan, K. Liu, H. J. Fan, S. W. Le, *ACS Energy Lett.* **2023**, *8*, 1.
[17] X. Zhang, L. Hu, K. Zhou, L. Zhang, X. Zeng, Y. Shi, W. Cai, J. Wu, Y. Lin, *Adv. Mater.* **2024**, *36*, 2412844.
[18] L. Jiang, Y. Li, Y. Cao, D. Gan, F. Zou, L. Yuan, D. Zhang, C. Xie, X. Lu, *Nano Lett.* **2025**, *25*, 2939.
[19] Y. Wang, F. Chen, Z. Liu, Z. Tang, Q. Yang, Y. Zhao, S. Du, Q. Chen, C. Zhi, *Angew. Chem., Int. Ed.* **2019**, *58*, 15707.
[20] Y. Zhou, C. Cao, Y. Cao, Q. Han, C. B. Parker, J. T. Glass, *Matter* **2020**, *2*, 1307.
[21] S. Feng, X. Wang, M. Wang, C. Bai, S. Cao, D. Kong, *Nano Lett.* **2021**, *21*, 7561.
[22] W. Wang, L. Gao, Z. Kong, B. Ma, M. Han, G. Wang, C. Li, *Adv. Mater.* **2023**, *35*, 2303353.
[23] Z. Lv, Y. Luo, Y. Tang, J. Wei, Z. Zhu, X. Zhou, W. Li, Y. Zeng, W. Zhang, Y. Zhang, D. Qi, S. Pan, X. J. Loh, X. Chen, *Adv. Mater.* **2018**, *30*, 1704531.
[24] Y. Diao, R. Woon, H. Yang, A. Chow, H. Wang, Y. Lu, J. M D'Arcy, *J. Mater. Chem. A* **2021**, *9*, 9849.
[25] P. Li, Z. Jin, L. Peng, F. Zhao, D. Xiao, Y. Jin, G. Yu, *Adv. Mater.* **2018**, *30*, 1800124.
[26] B. Dahal, B. Chhetri, A. Muthurasu, T. Mukhiya, A. P. Tiwari, J. Gautam, J. Y. Lee, D. C. Chung, H. Y. Kim, *Adv. Energy Mater.* **2020**, *11*, 2002961.
[27] Y. Zhao, B. Zhang, B. Yao, Y. Qiu, Z. Peng, Y. Zhang, Y. Alsaid, I. Frenkel, K. Youssef, Q. Pei, X. He, *Matter* **2020**, *3*, 1196.
[28] Y. Liu, H. Zhou, W. Zhou, S. Meng, C. Qi, Z. Liu, T. B. Kong, *Adv. Energy Mater.* **2021**, *11*, 2101329.
[29] H. Mu, W. Wang, L. Yang, J. Chen, X. Li, Y. Yuan, X. Tian, G. Wang, *Energy Storage Mater.* **2021**, *39*, 130.
[30] Q. Xie, C. Yi, H. Zhang, H. Xia, G. Xu, C. Miao, L. Yang, T. Shui, W. Zhang, Z. Sun, *Adv. Energy Mater.* **2024**, *14*, 2303592.
[31] H. Sun, J. Zhu, D. Baumann, L. Peng, Y. Xu, I. Shakir, Y. Huang, Z. Duan, *Nat. Rev. Mater.* **2019**, *4*, 45.
[32] Y. Kuang, C. Chen, D. Kirsch, L. Hu, *Adv. Energy Mater.* **2019**, *9*, 1901457.

[33] Y. Zhang, R. Zhang, S. Chen, H. Gao, M. Li, X. Song, H. L. Xin, Z. Chen, *Adv. Funct. Mater.* **2020**, *30*, 2005956.

[34] Y. Chen, M. Yousaf, Y. Wang, Z. Wang, S. Lou, R. P. S. Han, Y. Yang, A. Cao, *Nano Energy* **2020**, *78*, 105265.

[35] M. White, M. Choi, B. Hu, S. Chandrasekaran, X. Xue, M. Worsley, Y. Li, B. Dunn, *Adv. Mater.* **2025**, https://doi.org/10.1002/adma.202417128.

[36] H. Sun, L. Mei, J. Liang, Z. Zhao, C. Lee, H. Fei, M. Ding, J. Lau, M. Li, C. Wang, X. Xu, G. Hao, B. Papandrea, I. Shakir, B. Dunn, Y. Huang, X. Duan, *Science* **2017**, *356*, 599.

[37] D. G. Mackanic, M. Kao, Z. E. D. Bao, S. Batteries, *Adv. Energy Mater.* **2020**, *10*, 2001424.

[38] W. Yang, I. H. Chen, B. Gludovatz, E. A. Zimmermann, R. O. Ritchie, M. A. Meyers, *Adv. Mater.* **2013**, *25*, 31.

[39] I. H. Chen, J. H. Kiang, V. Correa, M. I. Lopez, P.-Y. Chen, J. McKittrick, M. A. Meyers, *J. Mech. Behav. Biomed.* **2011**, *4*, 713.

[40] S. Rudykh, C. Ortiz, M. C. Boyce, *Soft Matter* **2015**, *11*, 2547.

[41] R. Martini, Y. Balit, F. Barthelat, *Acta Biomater.* **2017**, *55*, 360.

[42] J. Shin, J. Ko, S. Jeong, P. Won, Y. Lee, J. Kim, S. Hong, N. L. Jeon, S. H. Ko, *Nat. Mater.* **2021**, *20*, 100.

[43] K. Zhang, S. Kong, Y. Li, M. Lu, D. Kong, *Lab Chip* **2019**, *19*, 2709.

[44] H. Luo, Y. Lu, Y. Xu, G. Yang, S. Cui, D. Han, Q. Zhou, X. Ouyang, H. Yang, T. Cheng, K. Xu, *Nano Energy* **2022**, *103*, 107803.

[45] A. Chortos, G. I. Koleilat, R. Pfattner, D. Kong, P. Lin, R. Nur, T. Lei, H. Wang, N. Liu, Y.-C. Lai, M.-G. Kim, J. W. Chung, S. Lee, Z. Bao, *Adv. Mater.* **2016**, *28*, 4441.

[46] Y. Zhou, S. Cao, J. Wang, H. Zhu, J. Wang, S. Yang, X. Wang, D. Kong, *ACS Appl. Mater. Interfaces* **2018**, *10*, 44760.

[47] Y. Jiang, Z. Zhang, Y.-X. Wang, D. Li, C.-T. Coen, E. Hwaun, G. Chen, H.-C. Wu, D. Zhong, S. Niu, W. Wang, A. Saberi, J.-C. Lai, Y. Wu, Y. Wang, A. A. Trotsyuk, K. Y. Loh, C.-C. Shih, W. Xu, K. Liang, K. Zhang, Y. Bai, G. Gurusankar, W. Hu, W. Jia, Z. Cheng, R. H. Dauskardt, G. C. Gurtner, J. B.-H. Tok, K. Deisseroth, et al., *Science* **2022**, *375*, 1411.

[48] D. Gan, Z. Huang, X. Wang, D. Xu, S. Rao, K. Wang, F. Ren, L. Jiang, C. Xie, X. Lu, *Mater. Horiz.* **2023**, *10*, 2169.

[49] Y. Zhu, S. Murali, M. D. Stoller, K. J. Ganesh, W. Cai, P. J. Ferreira, A. Pirkle, R. M. Wallace, K. A. Cychosz, M. Thommes, D. Su, E. A. Stach, R. S. Ruoff, *Science* **2011**, *332*, 1537.

[50] Y. Xu, Z. Lin, X. Zhong, X. Huang, N. O. Weiss, Y. Huang, X. Duan, *Nat. Commun.* **2014**, *5*, 4554.

[51] K. Kostarelos, A. Bianco, M. Prato, *Nat. Nanotechnol.* **2009**, *4*, 627.

[52] S. K. Smart, A. I. Cassady, G. Q. Lu, D. J. Martin, *Carbon* **2006**, *44*, 1034.

[53] Y. Jiang, Z. Zhang, D. Chen, J. Du, Y. Yang, S. Wang, F. Guo, X. Chen, C. Gao, W.-J. Wang, P. Liu, *Adv. Mater.* **2022**, *34*, 2204250.

[54] Y. Katsuyama, N. Haba, H. Kobayashi, K. Iwase, A. Kudo, I. Honma, R. B. Kaner, *Adv. Funct. Mater.* **2022**, *32*, 2201544.

[55] L. Manjakkal, A. Pullanchiyodan, N. Yogeswaran, E. S. Hosseini, R. Dahiya, *Adv. Mater.* **2020**, *32*, 1907254.

[56] W. Chen, Y. He, W. Gao, *J. Electrochem. Soc.* **2010**, *157*, E122.

[57] H.-M. Cheng, F. Li, *Science* **2017**, *356*, 582.

[58] W. Guo, C. Yu, S. Li, J. Qiu, *Energy Environ. Sci.* **2021**, *14*, 576.

[59] S.-H. Park, P. J. King, R. Tian, C. S. Boland, J. Coelho, C. Zhang, P. McBean, N. McEvoy, M. P. Kremer, D. Daly, J. N. Coleman, V. Nicolosi, *Nat. Energy* **2019**, *4*, 560.

[60] H. Cho, B. Lee, D. Jang, J. Yoon, S. Chung, Y. Hong, *Mater. Horiz.* **2022**, *9*, 2053.

[61] C.-C. Kim, H.-H. Lee, K. H. Oh, J.-Y. Sun, *Science* **2016**, *353*, 682.

[62] Y. Song, K. Chen, S. Chen, L. Zhang, Y. Wang, K. Wu, C. Xu, B. Li, J. Zhang, G. Liu, J. Sun, *Mater. Horiz.* **2025**, *12*, 1981.

[63] S. Wang, Y. Nie, H. Zhu, Y. Xu, S. Cao, J. Zhang, Y. Li, J. Wang, X. Ning, D. Kong, *Sci. Adv.* **2022**, *8*, abl5511.

[64] Q. Shen, M. Jiang, R. Wang, K. Song, M. H. Vong, W. Jung, F. Krisnadi, R. Kan, F. Zheng, B. Fu, P. Tao, C. Song, G. Weng, B. Peng, J. Wang, W. Shang, M. D. Dickey, T. Deng, *Science* **2023**, *379*, 488.

[65] G. Lee, J. W. Kim, H. Park, J. Y. Lee, H. Lee, C. Song, S. W. Jin, K. Keum, C.-H. Lee, J. S. Ha, *ACS Nano* **2019**, *13*, 855.

[66] A. Chen, X. Guo, S. Yang, G. Liang, Q. Li, Z. Chen, Z. Huang, Q. Yang, C. Han, C. Zhi, *Energy Environ. Sci.* **2021**, *14*, 3599.

[67] K. Dong, G. Zan, J. Zhou, F. Manshaii, S. Pu, S. Chai, J. M. Baik, Q. Wu, M. Wen, T. Wu, J. Chen, *Adv. Funct. Mater.* **2024**, *34*, 2408348.

[68] Z. Xie, R. Avila, Y. Huang, J. A. Rogers, *Adv. Mater.* **2020**, *32*, 1902767.

[69] Y. Wang, J. Wang, S. Cao, D. Kong, *J. Mater. Chem. C* **2019**, *7*, 9748.

[70] Y. Li, S. Wang, J. Zhang, X. Ma, S. Cao, Y. Sun, S. Feng, T. Fang, D. Kong, *ACS Appl. Mater. Interfaces* **2022**, *14*, 13713.

[71] Q. Lu, Y. Sun, M. Wu, Q. Wang, S. Feng, T. Fang, G. Hu, W. Huang, Z. Li, D. Kong, X. Wang, Y. Lu, *ACS Nano* **2024**, *18*, 13049.